Assessing the cardiac function from micro-gravity to hyper-gravity conditions through a validated multiscale modelling approach

First author profile

Francesco Tripoli is a Ph.D. student in Aerospace Engineering at Politecnico di Torino. He completed his MD in Biomedical Engineering at Politecnico di Torino in 2022. From October 2022 to October 2023, he received a post-graduate research scholarship at Politecnico di Torino. During this period, he applied numerical methods to investigate cerebral hemodynamics in atrial fibrillation. His current research focuses on both cardiovascular and cerebro-ocular functions under spaceflight conditions, exploiting mathematical multiscale modeling. His work aims to enhance the comprehension of cardiovascular and cerebral deconditioning during long-term human spaceflight and to support the identification of effective countermeasure strategies.

Key Points

Assessing the cardiac function from micro-gravity to hyper-gravity conditions through a validated multiscale modeling approach

Francesco Tripoli, Luca Ridolfi, Stefania Scarsoglio

- Gravity changes from micro- to hyper-gravity induce several cardiovascular alterations, from fluid shift and blood volume reduction to orthostatic hypotension and venous pooling.
- Although the overall cardiovascular response is clear, details of the cardiac function in these extreme conditions are still incomplete and difficult to obtain.
- We propose a validated multiscale cardiovascular model to investigate the steady-state acute cardiac response to gravity changes (from 0*g* to 3*g*).
- After a thorough validation against the most common central hemodynamic parameters in literature, present results show: (i) a different behaviour between left and right heart hemodynamics; (ii) an improvement of cardiac efficiency and cardiac performance in micro-gravity; (iii) an energy supply/demand impairment in hyper-gravity.
- The computational approach is a useful and reliable tool in exploring the response of cardiac parameters which are difficult to investigate experimentally, aiming to shed light on the cardiac function under altered gravitational force.

Assessing the cardiac function from micro-gravity to hyper-gravity conditions through a validated multiscale modeling approach

Francesco Tripoli[a], Luca Ridolfi[b, c] and Stefania Scarsoglio[a, c]

[a] *Department of Mechanical and Aerospace Engineering, Politecnico di Torino, Corso Duca degli Abruzzi 24, Turin, 10129, Italy*
[b] *Department of Environmental, Land and Infrastructure Engineering, Politecnico di Torino, Corso Duca degli Abruzzi 24, Turin, 10129, Italy*
[c] *PolitoBioMed Lab, Politecnico di Torino, Corso Duca degli Abruzzi 24, Turin, 10129, Italy*

Abstract

Gravity changes with respect to the 1*g* terrestrial condition induce several cardiovascular alterations, from fluid shift and blood volume reduction to orthostatic hypotension and venous pooling. Micro-gravity and hyper-gravity exposure characterizes space missions and aeronautical flights, as well as terrestrial analogs such as centrifuges, bed rest studies, and parabolic flights. Despite a growing number of clinical measures is becoming available, cardiac function in these extreme conditions is still incomplete and difficult to be obtained. Thus, computational hemodynamics provides a powerful and reliable tool to understand the cardiac response.

We propose a 0D-1D multiscale cardiovascular model to investigate the steady-state acute cardiac response to gravity changes (from 0*g* to 3*g*). The model combines a 1D description of the coronary circulation and arterial tree, with a 0D parameterization of the peripheral microcirculation, the venous return, the cardiopulmonary and the cerebrovascular-ocular circulations. The

overall model is equipped with short-term regulation mechanisms, and accounts for gravity and posture changes.

After a thorough validation using measured data from literature involving the most common central hemodynamic parameters (i.e., *HR*, *MAP*, *SV* and *CO*), the model provides an in-depth description of the cardiac response from micro- (0*g*) to hyper-gravity (3*g*), highlighting: (i) a different behaviour between left and right heart hemodynamics; (ii) an improvement of cardiac efficiency and cardiac performance in micro-gravity; (iii) a worsening of cardiac efficiency and an energy supply/demand impairment both at heart and coronary levels in hyper-gravity. Therefore, the modeling approach proves to be an important tool in shedding light on space medicine.

Keywords: Space medicine, micro-gravity, hyper-gravity, cardiovascular modeling, cardiac hemodynamics

1. Introduction

One of the most challenging issues of human space exploration and aeronautical flights is the exposure of the human body to gravitational force changes. During spaceflights, astronauts experience a wide range of gravitational accelerations (*g*), from the weightlessness to the increased gravitational stress sustained during launch or re-entry/landing maneuvers. In addition, many terrestrial activities, from civil and military flights to skydiving or rollercoasters, expose the human body to varying levels of gravity force. Changes in gravitational acceleration induce a number of physiological adaptations affecting musculoskeletal, cardiovascular and neurovestibular systems (Buckey, 2006; Clément, 2011; Young & Sutton, 2021). The comprehension of these adaptations is crucial to ensure the health and safety

of astronauts during future space missions and to develop effective countermeasures against deconditioning in the space environment (Traon *et al.*, 2007; Hargens & Richardson, 2009; Hargens *et al.*, 2013; Tanaka *et al.*, 2017).

The cardiovascular system is greatly affected by gravitational acceleration, with deviations from terrestrial gravity eliciting a blood volume redistribution due to the gravity-dependent hydrostatic component of the blood pressure (Blomqvist & Stone, 1983). Despite the increasing number of studies on the cardiovascular response to gravity changes (Blaber *et al.*, 2010; Zhu *et al.*, 2015; Hughson *et al.*, 2018; Shen & Frishman, 2019; Norsk, 2020), hemodynamic characterization is still incomplete and restricted to a limited number of cardiac parameters. Although the acquisition of clinical measures is difficult, it is thought that the micro-gravity-induced fluid shift from the lower to the upper body is the main driver of cardiovascular deconditioning (Hargens & Richardson, 2009; Norsk, 2020) – characterized by total blood volume reduction, cardiac atrophy and reduced exercise capability (Arbeille *et al.*, 2001; Grigoriev *et al.*, 2011; Zhu *et al.*, 2015) – and Spaceflight Associated Neuro-Ocular Syndrome (SANS) – characterized by several neuro-ocular anomalies triggered by elevated intracranial pressure (Berdahl *et al.*, 2012; Taibbi *et al.*, 2013; Zhang & Hargens, 2018). Conversely, hyper-gravity elicits a fluid shift in the cranio-caudal direction, exerting significant orthostatic stress on the cardiovascular system, which may result in reduced venous return to the heart and impaired cerebral perfusion (Blomqvist & Stone, 1983; Shender *et al.*, 2003). Despite being a hazardous condition, some studies proposed that repetitive exposure to hyper-gravity may enhance

tolerance to orthostatic stress, leading to adaptive cardiovascular responses (Newman *et al.*, 1998; Convertino, 1998; Newman & Callister, 2008; Lalande & Buick, 2009), and that exposure to mild hyper-gravity may mitigate deconditioning induced by spaceflight hostile environment (Burton, 1988; Clément *et al.*, 2015). Hence, understanding the cardiovascular response to micro- and hyper-gravity environments is critical for the implementation of countermeasures to protect astronauts during long-term spaceflight.

Ground-based analogs – such as bed-rest studies (Traon *et al.*, 2007; Saveko *et al.*, 2023), parabolic flights (Karmali & Shelhamer, 2008; Shelhamer, 2016) and human centrifuges (Scott *et al.*, 2007; Goswami *et al.*, 2015) – represent the easiest way to study the effect of gravitational acceleration changes in a controlled environment. However, these analogs have some limitations: (i) in bed-rest studies, the gravitational force (which typically acts on the longitudinal axis) is exerted on the antero-posterior axis, thus not eliminating the body weight; (ii) in human centrifuges, a gravity gradient along the longitudinal (head-feet) axis is produced due to the radius-dependent centrifugal force achieved by steady rotation; (iii) in parabolic flights, the real micro- and hyper-gravity environments are reproduced only for a few seconds (Karmali & Shelhamer, 2008). Moreover, the challenge of monitoring and recording detailed clinical data of the cardiovascular system – which is a complex issue even in controlled environment conditions due to the intrinsic limitations of the current acquisition methodologies – is amplified by the several design constraints inherent to each analog.

Mathematical modelling may represent a feasible tool to investigate the cardiovascular response to gravity alterations and clarify physiological aspects

that are still unclear. The computational approach and, in particular, the multiscale modeling allow distinct elements of the cardiovascular system to be described effectively, by combining submodels with different levels of detail (from 0D to 3D models). Each compartment is able to reproduce the main hemodynamic features of a specific vascular region and different physiological mechanisms – such as short-term regulation mechanisms mediated by the autonomic system – can be implemented. Due to these properties, in recent years multiscale mathematical modeling has gained success to investigate the hemodynamic response to different cardiovascular diseases – e.g., cardiac arrhythmias and hemorrhages (Anselmino *et al.*, 2016; Canuto *et al.*, 2018; Saglietto *et al.*, 2024) – and working conditions where the gravitational acceleration plays a crucial role like head-up and head-down tilt tests and human centrifuge (Heldt *et al.*, 2002; Diaz-Artiles *et al.*, 2019; Whittle & Diaz-Artiles, 2021; Fois *et al.*, 2022*a*, 2024).

In this work, by exploiting a multiscale 0D-1D cardiovascular model, we describe the cardiac function in standing posture across a broad spectrum of gravity intensity: from micro-gravity (0*g*) to hyper-gravity (3*g*). In particular, the steady-state acute response – which is mediated by short-term regulation mechanisms and occurs within few minutes following the application of an external stimulus – is investigated. The model includes a 0D-1D modelling of the systemic and coronary circulation, a 0D model of the cerebrovascular circulation, and has been recently validated and used to investigate the cardiovascular and cerebro-ocular hemodynamics against different ground-based and spaceflight applications (Gallo *et al.*, 2020; Fois *et al.*, 2022*a*, 2022*b*, 2024).

After an in-depth validation through existing literature involving the most common central hemodynamic parameters, we study the cardiac response from micro- (0g) to hyper-gravity (3g) by focusing on: left and right heart hemodynamics (including central venous and pulmonary capillary wedge pressures), left and right coronary circulation (left anterior descending artery and right coronary artery), pulmonary artery pressure, and indexes of oxygen consumption, cardiac work and efficiency.

2. Methods

2.1. Mathematical modelling

The mathematical framework employed in this work is based on a closed-loop 0D-1D multiscale model of the entire cardiovascular system (Fois *et al.*, 2024). An overview of the model architecture is illustrated in figure 1. The cardiovascular model comprises a 1D description of the arterial tree along with the main coronary arteries and a 0D representation of the peripheral, venous, cardiopulmonary, coronary and cerebro-ocular circulations. In this section, a brief description of the model structure and the implemented physiological features is given, whereas additional numerical details, including equations and parameter settings, are reported in our previous work (Fois *et al.*, 2024) and are available through the link attached in the Additional Information section (please refer to the Supporting Information file).

The 1D arterial tree (left side of Fig. 1) consists of 48 main large arteries (from the ascending aorta to upper and lower limbs arteries) and 15 coronary arteries, for a total of 63 vessels. Each artery is modelled as a straight tapered vessel with a circular cross-section. Blood is modelled as an incompressible and Newtonian fluid with constant density ρ = 1050 kg/m^3 and viscosity μ =

$4 \cdot 10^{-3}$ Pa·s. These hypotheses permit the description of blood motion through the 1D axisymmetric form of the Navier-Stokes equations, taking the lumen area *A(x,t)* and the blood flow rate *Q(x,t)* as dependent variables (*x* is the axial vessel coordinate, and *t* is the time). To close the 1D mathematical system and to model the viscoelastic mechanical properties of the large artery walls, a non-linear constitutive equation associating the arterial blood pressure *p(x,t)* with *A(x,t)* is introduced (Fois *et al.*, 2024). The model accounts for the gravity force by explicitly including a properly orientated gravitational term in the momentum balance equation. At each arterial bifurcation, the conservation of mass and total pressure is imposed as boundary condition.

The inlet of the 1D ascending aorta is linked with the 0D aortic valve model, and each of the twenty-four 1D terminal arteries is coupled by means of a characteristic impedance Z_c with a three-element RLC Windkessel model of the 0D arteriolar compartment. Each boundary value problem is treated by applying the method of characteristics (Fois *et al.*, 2024). The 1D governing equations are solved numerically using the Discontinuous Galerkin Finite Elements method combined with a 2-step Runge-Kutta explicit time integration scheme.

The 0D model of the peripheral and venous circulations is characterized by several interconnected three-element RLC Windkessel models, with *R*, *L* and *C* describing the hydraulic resistance, the blood inertia, and the compliance of a specific 0D compartment, respectively. Specifically, arteriolar compartments merge into five body regions: extracranial circulation, arms, upper abdomen, lower abdomen and legs. Each of these regions comprises a capillary, venular and venous district. Three additional districts,

describing the superior, inferior and abdominal segments of the vena cava, connect the venous compartments with the right atrium, thus closing the systemic circulation and completing the venous return to the heart. For each compartment, the governing equations are written in terms of the flow rate $Q(t)$, the blood volume $V(t)$, and the intraluminal pressure $p(t)$. For legs venous and superior vena cava districts, two different non-linear pressure-volume relationships are implemented to model the non-linear effects of distending leg veins volume (Fois *et al.*, 2024) and venous collapse of neck veins (Lu *et al.*, 2001; Holmlund *et al.*, 2018). Additionally, arms and legs venous compartments are provided with a 0D model of venous valves. To insert gravity contribution a pressure generator is added in the venous and vena cava compartments according to Stevino's law.

The 0D model of the cardio-pulmonary circulation combines four 0D models, each describing a specific cardiac chamber, with a 0D model of the pulmonary circulation. To model the contraction of atria and ventricles a time-varying elastance is employed, whereas to model cardiac valves non-ideal diodes are used. Moreover, intrathoracic pressure (*ITP*), which depends on both gravity and body position (Fois *et al.*, 2022*a*), acts as extravascular pressure, affecting the behaviour of all compartments of the cardio-pulmonary circulation.

The cerebro-ocular circulation is connected with the systemic arterial circulation via the internal carotid and the vertebral arteries, whereas the venous outflow is directly connected to the superior vena cava compartment. The cerebral model (Fois *et al.*, 2024) describes the cerebral blood flow within the large cerebral arteries, the circle of Willis and the distal cerebral

circulation. Furthermore, it models the cerebrospinal dynamics and estimates the intracranial pressure (*ICP*) by imposing the mass conservation and assuming a non-linear intracranial compliance. The 0D model of the eye (Fois *et al.*, 2024) includes six ocular compartments and is able to reproduce both intraocular pressure (*IOP*) and ocular globe volume.

The whole cardiovascular model is equipped with short-term autonomic control mechanisms, simulating the baroreflex and the cardio-pulmonary reflex (Fois *et al.*, 2024). For both reflexes, sympathetic and parasympathetic activities are governed by two sigmoid functions (which depend on the mean aortic-carotid sinus pressure for the baroreflex, and the central venous pressure for the cardiopulmonary reflex). The baroreflex model regulates both peripheral resistances and venous tone and exerts an inotropic and chronotropic effect on both ventricles, whereas the cardiopulmonary reflex accounts only for peripheral vascular adjustments. Additionally, the 0D cerebral model accounts for the cerebral autoregulation mechanism by changing the compliances and the hydraulic resistances of the distal cerebral circulation. The implementation of these regulation mechanisms allows the model to simulate the short-term response to both posture and gravity changes.

To obtain the steady-state cardiovascular response in a standing posture, we first simulated a head-up tilt test at $1g$. In this first step, the time-dependence of the tilt angle α was computed as:

$$\alpha(t) = \begin{cases} 0, & \text{if } t < t_{start}^{I} \\ \frac{\alpha_{tilt}}{2} \cdot \left[1 - \cos\left(\frac{t - t_{start}^{I}}{T_{tilt}} \cdot \pi\right)\right], & \text{if } t_{start}^{I} < t < t_{start}^{I} + T_{tilt} \\ \alpha_{tilt}, & \text{if } t > t_{start}^{I} + T_{tilt} \end{cases} \quad (1)$$

where α_{tilt} represents the angle reached after the tilt (90°), t^{I}_{start} indicates the tilting starting time, and T_{tilt} denotes the tilting period in which the posture change occurred (22.5 s), respectively. Subsequently, starting from the standing 1g steady-state condition, gravity transitions from 1g up to the desired level of gravity were imposed by the cosinusoidal function:

$$\frac{g}{g_0}(t) = \begin{cases} 1, & \text{if } t < t^{II}_{start} \\ 1 + \frac{1}{2}\left[\left(\frac{g}{g_0}\right)_f - 1\right] \cdot \left[1 - \cos\left(\frac{t - t^{II}_{start}}{T_g} \cdot \pi\right)\right], & \text{if } t^{II}_{start} < t < t^{II}_{start} + T_g \\ \left(\frac{g}{g_0}\right)_f, & \text{if } t > t^{II}_{start} + T_g \end{cases} \quad (2)$$

where $\left(\frac{g}{g_0}\right)_f$, t^{II}_{start}, and T_g indicate the final gravity level reached after the transition, the transition starting time, and the transition duration, respectively. To simulate both posture and gravity changes, t_{start} was selected in order to ensure that the initial transient resulting from model initialization was fully extinguished. Additionally, to prevent numerical instabilities, in particular at higher g values, all simulations were performed with a fixed gravity rate of ±0.01 g/s. While this gravity rate may not reflect typical real-life applications, our study is focused on the short-term steady-state condition, which is independent of the gravity rate (Fois *et al.*, 2022*a*). A total of 31 simulations were conducted with g varying in the range [0g-3g].

Cardiac and coronary hemodynamic parameters

We here introduce the hemodynamic parameters used to describe the cardiac and coronary responses to gravity changes in the results section (see Section 4). To assess the cardiac function, we focus our attention on the main mechano-energetic and efficiency indexes of the left and right ventricles. In

particular, starting from each ventricle pressure-volume loop (*PV* loop) (see Fig. 3), it is possible to define the external work $EW_{lv/rv}$ [J] as the area of left/right *PV* loop, and the potential energy $PE_{lv/rv}$ [J] as the area of the triangles depicted in figures 3a and 3b (Westerhof *et al.*, 2019). An additional mechano-energetic parameter, which can be derived from $EW_{lv/rv}$ and $PE_{lv/rv}$, is the left/right ventricle pressure-volume area, $PVA_{lv/rv}$ [J], defined as:

$$PVA_{lv/rv} = EW_{lv/rv} + PE_{lv/rv}. \quad (3)$$

With regard to cardiac efficiency, left/right ventricular efficiency (*LVE* and *RVE*) and ejection fraction ($EF_{lv/rv}$) are considered:

$$LVE\ (or\ RVE) = \frac{EW_{lv/rv}}{PVA_{lv/rv}}, \quad (4)$$

$$EF_{lv/rv} = \frac{SV_{lv/rv}}{EDV_{lv/rv}}, \quad (5)$$

where $SV_{lv/rv} = EDV_{lv/rv} - ESV_{lv/rv}$ is the stroke volume [ml], that is the blood volume ejected from the left/right ventricle during a single cardiac cycle, $EDV_{lv/rv}$ [ml] is the left/right ventricle end-diastolic volume (defined by the closure of the mitral/tricuspid valve), and $ESV_{lv/rv}$ [ml] is the the left/right ventricle end-sistolic volume (defined by the closure of the aortic/pulmonary valve).

In literature, the most common methods to assess the cardiac oxygen consumption indexes – which are mainly based on pressure and heart rate – are the rate-pressure product (*RPP* [mmHg/min]) and the tension-time index (*TTI* [mmHg·s]), both defined as (Westerhof *et al.*, 2019):

$$RPP = P_{aa,sys} \cdot HR, \quad (6)$$

$$TTI = P_{lv,mean} \cdot RR, \quad (7)$$

where $P_{aa,sys}$, $P_{lv,mean}$, HR and RR are the aortic systolic pressure, the mean left ventricle pressure, the heart rate and the cardiac cycle duration ($HR = 60/RR$), respectively. In this study, since we are interested in the cardiac work and oxygen consumption expressed per minute, these mechano-energetic and oxygen consumption indexes, apart from RPP, are multiplied by HR (i.e., $EW_{lv/rv}/min$ [J/min], $PE_{lv/rv}/min$ [J/min], $PVA_{lv/rv}/min$ [J/min], and TTI/min [mmHg·s/min]).

To assess coronary perfusion at different levels of gravitational acceleration, two of the main branches of coronary circulation are investigated. Specifically, blood flows in the left anterior descending artery (LAD) – which is a branch of the left coronary artery and supplies blood to the anterior region of the left ventricle - and the right coronary artery (RCA) – which originates from the right aortic sinus and supplies blood to both the right ventricle and atrium – are evaluated. The analyzed hemodynamic parameters are the coronary stroke volume ($SV_{LAD/RCA}$ [ml]), the coronary blood flow ($CBF_{LAD/RCA}$ [ml/min]), and the coronary perfusion pressure ($CPP_{LAD/RCA}$ [mmHg]), which are respectively defined as follows:

$$SV_{LAD/RCA} = SV_{sys,LAD/RCA} + SV_{dia,LAD/RCA} =$$

$$= \int_{RR_{sys}} Q_{LAD/RCA}(t) \cdot dt + \int_{RR_{dia}} Q_{LAD/RCA}(t) \cdot dt\,, \tag{8}$$

where RR_{sys}, RR_{dia} are the systolic and diastolic intervals, and $Q_{LAD/RCA}$ is the flow rate within the LAD/RCA artery; and

$$CBF_{LAD/RCA} = SV_{LAD/RCA} \cdot HR, \tag{9}$$

$$CPP_{LAD/RCA} = P_{aa,dia} - EDP_{lv/rv}, \tag{10}$$

with $P_{aa,dia}$ being the diastolic aortic pressure.

3. Model validation

The existing literature provides very limited data on short-term cardiac response to actual spaceflight conditions of micro- and hyper-gravity. In particular, the hemodynamic parameters associated with the right heart, along with metrics for oxygen consumption, and coronary and cerebro-ocular circulations are poorly understood in both micro- and hyper-gravity environments. To validate our model, we relied on experimental measurements extracted from parabolic flight and centrifuge studies (Fontolliet *et al.*, 2015; Ueda *et al.*, 2015; Habazettl *et al.*, 2016; Ogawa *et al.*, 2016; Diaz-Artiles *et al.*, 2018; Konishi *et al.*, 2019) (please, refer to the link in the Additional Information section for raw data about the validation dataset constructed from experimental measures extracted from the literature). In order to enlarge the validation dataset, parabolic flight campaigns assessing both standing (Lathers *et al.*, 1989; Mukai *et al.*, 1991; Caiani *et al.*, 2006, 2007; Liu *et al.*, 2012) and sitting postures (Norsk *et al.*, 1987, 2006; Pump *et al.*, 1999; Beckers *et al.*, 2003; Petersen *et al.*, 2011; Ogoh *et al.*, 2015; Widjaja *et al.*, 2015; Klein *et al.*, 2019) were included. Parabolic flights expose the cardiovascular system to a sequence of hyper-gravity and micro-gravity phases, each lasting only a few seconds, during which accelerations of 1.8*g* and 0*g* are typically reached. Human centrifuge studies achieve higher *g*-forces, thereby allowing us to extend the validation dataset to the gravity range [0*g*-2.5*g*]. However, it should be noted that, as it happens in real space- and aeronautical flight conditions, our model correctly reproduces a uniform gravitational acceleration along the longitudinal axis, whereas centrifuge-induced hyper-gravity entails a gravity acceleration gradient along the head-

feet axis (or *z*-axis). Moreover, in the considered experimental datasets the radius of the centrifuge varied between 1.4 m and 7.2 m; this results in different acceleration gradients along the body (in different centrifuges) for the same reference value at a given point on the body itself. Finally, the reference point along the *z*-axis for the acceleration measure was not uniform across studies: some of them report it at heart level (Ueda *et al.*, 2015; Ogawa *et al.*, 2016; Konishi *et al.*, 2019) and others at foot level (Habazettl *et al.*, 2016; Diaz-Artiles *et al.*, 2018). Due to the aforementioned differences, the experimental data exploited to validate our model are inherently heterogeneous.

The model was validated against the experimental behaviour of six hemodynamic variables – which are the most commonly reported variables in the literature – in the gravity range from 0*g* to 2.5*g*. The variables considered are: heart rate (*HR* [bpm]), cardiac output (*CO* [l/min]), stroke volume (*SV* [ml]) mean arterial pressure (*MAP* [mmHg]), systolic arterial pressure (*SAP* [mmHg]), and diastolic arterial pressure (*DAP* [mmHg]). It is worth noting that both in centrifuge and parabolic flight studies, all authors measured the arterial blood pressure at the level of the finger. These measurements were corrected either by maintaining the hand at the same level of the heart or applying an appropriate pressure correction that accounts for the contribution of the hydrostatic term. In addition, some of these authors computed *MAP*, *SAP* and *DAP* after reconstructing the brachial artery pressure via a suitable transfer function. Conversely, in our model, *MAP*, *SAP* and *DAP* are computed at the level of the ascending aorta.

For each group of the dataset (centrifuges, parabolic flights at seated and standing posture), all hemodynamic variables were normalized with respect to the corresponding 1g values (the normogravity 1g condition is denoted as g_0). This normalization eliminates the heterogeneity in baseline mean values at 1g across individual studies, ensuring a direct focus on how each cardiac parameter changes with g. Following normalization, the experimental data of each variable collected from the literature were pooled. In particular, the data pooling was carried out across each investigated gravity level. For instance, considering that centrifuge studies provided *HR* measurements at g/g_0 = [0, 0.5, 1, 1.4, 1.5, 2, 2.5], the pooled mean (μ^p) and the pooled standard deviation (σ^p) were computed for each of these g values. It is important to note that the number of observations for each sample varies across the different studies. Therefore, values of μ^p and σ^p for each cardiac parameter X and gravity level j were computed as (Borenstein *et al.*, 2009):

$$\mu_{Xj}^{p} = \frac{\sum_{i=1}^{k} n_i \, \mu_{Xi,j}}{\sum_{i=1}^{k} n_i}, \tag{11}$$

$$\sigma_{Xj}^{p} = \sqrt{\frac{\sum_{i=1}^{k} \sigma_{Xi,j}^{2} \, (n_i - 1) + \sum_{i=1}^{k} n_i \left(\mu_{Xi,j} - \mu_{Xj}^{p}\right)^2}{\sum_{i=1}^{k} n_i - 1}}, \tag{12}$$

where n_i, $\mu_{Xi,j}$, $\sigma_{Xi,j}$ denote the number of samples, the mean, and standard deviation for the *X-th* cardiac parameter, at gravity level j, in the literature study i, respectively. Additionally, it should be mentioned that due to differences in experimental protocols, methods, and purposes among the extracted literature studies, not all provided experimental measurements for every cardiac parameter at each gravity level investigated. This heterogeneity

resulted in a fragmented dataset, which did not allow for the computation of μ^p_{Xj} and σ^p_{Xj} for certain cardiac parameters at specific g values. In particular, experimental measurements for *SV* and *CO* are missing at 2.5g, while data for *SAP* and *DAP* are not given at 0.5g. After determining the values of μ^p_{Xj} and σ^p_{Xj} for each cardiac variable, a linear regression using the weighted least-squares fitting method was performed to verify the existence of a statistically significant trend with g. This approach enabled us to consider the impact of the different σ^p_{Xj} across the data by applying the weights $w_j = 1/(\sigma^p_{Xj})^2$ in the formula for the sum of squared errors (Neter *et al.*, 1996). Statistical significance of each trend was determined using a two-sided t-test for the slope coefficient, with a significance level of 0.05.

Figure 2 shows, for each parameter, the model outcomes and the regression lines (dashed curves) alongside the pooled means μ^p_{Xj} and the pooled standard deviation values σ^p_{Xj} (horizontal lines) of each dataset group collected from the literature.

Experimental data reveal an increasing trend in *HR*, *MAP*, *SAP*, and *DAP*, while *SV* and *CO* exhibit a decreasing behaviour. In particular, the linear regression analysis confirms that the trends in *HR*, *MAP*, *SAP*, *DAP*, and *SV* are statistically significant (p-value < 0.05), whereas *CO* fails to pass the t-test, reporting a p-value of 0.13. In detail, as gravity increases from 0g to 2g, centrifuges data (red lines) show a -37.8% decrease in μ^p_{SV}. Similarly, parabolic flight measures indicate reductions of -39.5% and -29.8% in the range [0g-1.8g] in standing (blue lines) and sitting positions (yellow lines), respectively (Fig. 2a). This behaviour is attributed to the fact that an increase in g triggers a fluid shift from the upper to lower regions of the body, leading

to decreased venous return and reduced *SV*. To counteract this drop, short-term regulation mechanisms (arterial baroreflex and cardiopulmonary reflex) induce a rise in μ^p_{HR} (Fig. 2b): +57% from 0*g* to 2.5*g*, +33% and +12.8% from 0*g* to 1.8*g* in parabolic flights with standing and seated posture, respectively. As a result, *CO* remains relatively stable within the investigated range of gravity, explaining the non-significant trend in *CO* (Fig. 2c).

Observing the pressure data, systemic *MAP* (Fig. 2d) appears to increase with increasing gravitational force – μ^p_{MAP} rises by 11.2%, 16.2% and 16.8% for centrifuges, parabolic flight in standing and seated posture, respectively – mostly due to increased μ^p_{DAP} (Fig. 2e). With regard to *SAP*, the experimental data show some discrepancies. Specifically, μ^p_{SAP} (Fig. 2f) does not exhibit a clear trend in relation to gravity in centrifuge measures (red lines). Conversely, during parabolic flights, an increase of +19% is observed from 0*g* to 1.8*g* in the sitting position (yellow lines), whereas in the standing posture (blue lines), the initial elevation occurring from 0*g* to 1*g* is followed by a slight decline in the hyper-gravity range.

Our cardiovascular model gives values which generally align with the experimental data, and all model outcomes (reported in Fig. 2 through solid black curves) fall within the range $\mu^p \pm \sigma^p$, indicating that the model is able to capture the cardiovascular response to gravity changes in both micro- and hyper-gravity conditions. In particular, *SV* (panel a) decreases by -46.1% within the range [0*g*-2*g*], in agreement with experimental data, and drops by -60.8% up to 3*g*, varying from 82.9 ml at 0*g* to 32.5 ml at 3*g*. Conversely, *HR* (panel b) initially exhibits a non-linear increase from 0*g* to 0.5*g*, followed by a linear behaviour beyond this value. Specifically, as gravitational

acceleration varies from 0*g* to 3*g*, the model detects an increment of 94%, with *HR* growing from 66 bpm to 128 bpm. Moreover, a good correspondence between the predicted values for both *SV* and *HR* and their respective regression lines is observed. With regard to *CO* (panel c), the model predicts a slight monotonic decrease from 5.45 l/min at 0*g* to 4.16 l/min at 3*g* (-23.7%). Notably, although the weighted least-squares fitting analysis highlighted a weakly non-significant trend for *CO*, the slope of the data-based regression line is negative and closely aligns with the results provided by the model.

Due to the peripheral vascular adjustments governed by short-term regulation mechanisms, *MAP* (panel d) mildly increases from 92 mmHg at 0*g* to 96.2 mmHg at 1*g* (+4.6%). Beyond this value, *MAP* remains constant up to 2.2*g*, before gradually decreasing and returning to 92 mmHg at 3*g*. The model correctly predicts the increase in diastolic pressure (panel e). In particular, *DAP* grows monotonically from 0*g* to 2.5*g*, varying from 69 mmHg to 82 mmHg (+19%), while it remains quite constant from 2.5*g* to 3*g*. Concerning *SAP* (panel f), the model predicts a non-monotonic behaviour with *g*. The systolic pressure is constant at around 121 mmHg in the gravity range [0*g*-0.5*g*]. Beyond this range, *SAP* exhibits a monotonic decrease, reaching a value of 104 mmHg at 3*g*. This behaviour doesn't fully match with the fitting analysis, where a positive slope was found for *SAP*. However, as above-mentioned, the experimental data are quite contradictory, and a decline in *SAP* is also observed during the hyper-gravity phase of parabolic flight in a standing posture (blue symbols). We recall that this posture, among all the experimental setups examined, is the most representative of that simulated by

our model, which reproduces a uniform gravitational acceleration along the head-feet axis during exposure to gravity transitions in standing posture.

4. Results

The previous section allowed us to validate and compare our cardiovascular model with existing experimental data of the main central hemodynamic variables. Here, by means of our mathematical model, we will explore the response of cardiac parameters which are difficult to investigate experimentally, aiming to shed light on the cardiac function under altered gravitational force. In particular, the short-term cardiac response to gravity changes will be first investigated by means of the main mechano-energetic cardiac parameters and oxygen consumption indexes. Secondly, the perfusion of the myocardial tissue will be examined by focusing on both the left and right coronary circulations. Finally, the gravity impact on mean and pulsatile values of the central venous pressure (*CVP*), the pulmonary artery pressure (P_{pa}), the pulmonary capillary wedge pressure (*PCWP*), and the central aortic pressure (P_{aa}) will be evaluated.

Figure 3 illustrates the acute hemodynamic response of the left and right ventricles from micro- (0*g*) to hyper-gravity (3*g*). In particular, the response is investigated in terms of the cardiac parameters introduced in the Section 2.2.

The right and left ventricles *PV* loops (Fig. 3a and 3b) exhibit significantly different responses to gravity changes. As *g* varies from 0*g* to 3*g*, due to the reduced venous return at higher *g* values, both left and right end-diastolic volumes ($EDV_{lv/rv}$) decrease similarly between the two ventricles, with EDV_{lv} and EDV_{rv} varying from 133.0 ml to 67.7 ml and from 143.0 ml to

65.6 ml, respectively. A reduction in left and right end-systolic volumes ($ESV_{lv/rv}$) is also observed as *g* rises: ESV_{lv} decreases from 50.1 ml at 0*g* to 35.2 ml at 3*g*, whereas ESV_{rv} diminishes from 60.7 ml to 33.8 ml. Additionally, due to the reduced ventricular filling both left and right ventricular end-diastolic pressures ($EDP_{lv/rv}$) decrease monotonically with increasing *g*. However, this similar behaviour between the ventricles does not apply to end-systolic pressures ($ESP_{lv/rv}$). In the systemic circulation, the baroreceptors and cardiopulmonary reflexes induce an increase in total peripheral resistance, maintaining an adequate ESP_{lv} even at higher *g* values, with ESP_{lv} slightly decreasing from 96.6 mmHg at 0*g* to 86.6 mmHg at 3*g*. On the contrary, in the right ventricle, ESP_{rv} decreases from 15.1 mmHg at 0*g* to 2.23 mmHg at 3*g* (-85%). This entails a different behaviour of *EW/min* between the left and right ventricles (Fig. 3c and 3d). In particular, the decrease in *EDV*, elicited by the blood shift towards the lower extremities and the reduced venous return, affects the preload, reducing both the stroke volume and the *EW* via the Frank-Starling mechanism (Westerhof *et al.*, 2019). However, while for the left ventricle, the *PV* loop shrinks primarily in a horizontal direction, thus limiting the reduction in *EW/min*, this does not occur for its right counterpart, where both a horizontal and vertical shortening of the *PV* loop is detected. Hence, the reduction in *EW/min* for the left ventricle is restricted to -15% up to 2.2*g* (from 76 J/min at 0*g* to 65 J/min at 2.2*g*). Beyond this value, *EW/min* decreases with a higher rate and a drop of -27% is detected at 3*g* with respect to 0*g*. Conversely, the rate of decrease in *EW/min* is almost constant for the right ventricle, and a reduction of -47% is observed as gravity rises from 0*g* to 3*g* (from 11.8 J/min to 6.2 J/min).

Differences between the right heart and the left heart are also noticeable in *PE/min*. In the left ventricle, the mechanical potential energy expressed per minute (Fig. 3c) does not exhibit large variations. In particular, it displays a non-monotonic trend, gradually increasing with gravitational acceleration and reaching a maximum at around 2.3*g* (from 21.5 J/min at 0*g* to 27.6 J/min at 2.3*g*, +28.4%). Beyond this peak, *PE/min* declines slightly, but remains higher compared to the value observed at 0*g*. In contrast, in the right ventricle, *PE/min* decreases monotonically from 4.4 J/min at 0*g* to 2.4 J/min at 3g (-45.5%), due to the abovementioned decline in ESP_{rv}.

Pressure-volume area *PVA/min*, which is given by the sum of *PE/min* and *EW/min* (see shaded areas in panels 3a-b), follows a similar response to that of *EW/min* in both ventricles. The strong dependence of *PVA/min* on *EW/min* is primarily due to the minor variations in *PE/min* with respect to the changes in *EW/min* as gravity rises. However, by observing the efficiency indexes *LVE* and *RVE* (Fig. 3e and 3f) – which are defined as the ratio *EW/PVA* – two different responses to gravity changes between left and right ventricles emerge due to the different behaviour of *PE/min*. In the left heart chamber, *LVE* decreases monotonically from 0.78 at 0*g* to 0.68 at 3*g* (-12.8%), whereas *RVE* is almost constant, varying from 0.73 to 0.72 (-1.4% from 0*g* to 3*g*).

In figures 3e and 3f, another index of cardiac efficiency, *EF*, is reported. *EF* expresses the emptying capability of the left/right ventricle during systole. This capability worsens similarly for both ventricles as gravity rises. The primary reason behind this decline is the reduction in *SV* (see Fig. 2a), which is equal for right and left ventricles. In particular, as gravity rises from 0*g* to

3*g*, *EF* decreases from 62% to 48% in the left ventricle and from 58% to 48% in the right one.

Finally, figure 3g illustrates the behaviours of the oxygen consumption indexes *RPP* and *TTI/min*. Both indexes exhibit a non-linear increase with *g*. *TTI/min* is characterized by a minimum in the proximity of 0.4*g*, followed by a central section where *TTI/min* increases, reaching a maximum close to 2.7*g*. However, as already observed in a previous study on the cardiovascular response to parabolic flights (Fois *et al.*, 2022*b*), *TTI/min* remains slightly affected by gravitational acceleration, with variations across the gravity range limited to -0.6% (at 0.4*g*) and to +7.7% (at 2.7*g*) with respect to the 0*g* condition. Conversely, *RPP* shows a +68.5% increase within the range [0*g*-3*g*]. Hence, the behaviours of both *TTI/min* and, especially, *RPP* suggest an increase in oxygen consumption and, therefore, in energy demand of the left ventricle at higher *g* values. Moreover, being *EW/min* an index of the energy supply, the comparison of *EW/min* and oxygen consumption indexes highlights a mismatch between the left ventricle energy supply and energy demand for increasing gravity levels.

In figure 4, the comparison between the short-term hemodynamic response of the left and right coronary circulations is reported. Coronary perfusion is evaluated at varying levels of gravitational acceleration in terms of coronary $SV_{LAD/RCA}$, $CBF_{LAD/RCA}$ and $CPP_{LAD/RCA}$ (see Section 2.2). Additionally, the LAD flow rate (Q_{LAD}) waveforms at four different levels of *g* are reported.

Figure 4a displays SV_{LAD}, SV_{RCA} and their SV_{LAD}/SV_{RCA} ratio. *SV* varies similarly with gravity in both LAD and RCA. Thus, the SV_{LAD}/SV_{RCA} ratio is

497 barely affected by gravity changes, varying from 1.54 at 0*g* to 1.42 at 3*g* (-
498 7.8%). Specifically, at low *g* values, a slight increment in *SV* is observed,
499 which reaches a maximum in the proximity of 0.5*g*. Beyond this value, *SV*
500 sharply decreases, falling by -26.8% and -32.4% from 0*g* to 3*g* in the RCA
501 and LAD, respectively. This drop is primarily due to the increase in *HR* with
502 *g*. In fact, as *HR* increases, the duration of the cardiac cycle (*RR*) reduces,
503 leading to altered diastolic and systolic lengths (RR_{dia} and RR_{sys}). It follows
504 that – as blood flow within the coronary arteries occurs mainly during diastole
505 due to the mechanical compression exerted by the cardiac muscle in the
506 systolic phase – the coronary perfusion changes. In particular, diastolic length
507 suffers a more significant contraction compared to systole (RR_{dia} is 59.8% of
508 *RR* at 0*g* and 43.3% of *RR* at 3*g*), resulting in a decreased RR_{dia}/RR_{sys} ratio and
509 a reduced *SV*. This response is well captured in figures 4b and 4c, where the
510 fractions of *SV* during diastolic and systolic phases (SV_{dia} and SV_{sys}) in LAD
511 and RCA are reported at different levels of *g*: while SV_{sys} is almost constant
512 throughout the gravity range both in LAD and RCA, SV_{dia} mirrors the same
513 behaviour of total *SV*. Hence, the SV_{dia}/SV_{sys} ratio decreases with *g*, varying
514 from 3.7 at 0*g* to 1.7 at 3*g* in the LAD, and from 1.5 and 1.1 in the RCA.
515 Despite an overall decrease in *SV* is observed as *g* rises, *CBF* (Fig. 4d)
516 grows with *g* in both coronary arteries due to the rise in *HR*. However, *CBF*
517 exhibits a non-linear trend characterized by a downward concavity which
518 reduces its increase at higher *g* values: in the LAD, an increase of +31.7% is
519 detected at 3*g* with respect to 0*g*, whereas *CBF* rises by 42.5% in the RCA.
520 Additionally, recalling that an increase in *RPP* of +68.5% is detected at 3*g*
521 (recall panel 3d), the non-linear behaviour of *CBF* suggests an imbalance of

522 the energy supply/demand ratio even at coronary level during hyper-gravity
523 exposure.
524 *CPP* (in Fig. 4e) displays a similar behaviour to that of *CBF* in both
525 coronary arteries. We recall that, *CPP* is often used as a surrogate for *CBF*
526 (Koeppen & Stanton, 2023). According to its formulation, *CPP* is strictly
527 associated with aortic diastolic pressure. Therefore, the increment in *DAP* with
528 *g* is the main cause of *CPP* behaviour. Moreover, the CPP_{LAD}/CPP_{RCA} ratio is
529 constant throughout the gravity range and is equal to 0.93 (not shown in Fig.
530 4e), thus highlighting no impairment between right and left *CPP* as *g* varies.
531 Figure 4f highlights the impact of *g* on Q_{LAD} by showing the flow rate
532 waveforms at four different levels of *g* (0*g*, 1*g*, 2*g* and 3*g*). As *g* increases
533 from 0*g* to 3*g*, the waveform undergoes significant changes mainly during
534 diastole. In fact, besides a temporal shortening due to the rise in *HR*, an
535 amplitude stretch is observed, with the diastolic peak growing with rising *g*.
536 At lower *g* values, the diastolic maximum peak is followed by a slow
537 decreasing phase. This feature is completely lost at higher *g* due to the
538 contraction of the diastole duration. Consequently, the systole begins with
539 significantly higher Q_{LAD} values. This is the most significant change that can
540 be detected during the systolic phase. Additionally, figures 4g and 4h illustrate
541 how the length of the cardiac cycle affects the SV_{dia}/SV_{sys} ratio as *g* varies from
542 0*g* to 3*g*. The impact of *HR* on the imbalance of the RR_{dia}/RR_{sys} ratio is clearly
543 observed, with the ratio decreasing from 1.49 at 0*g* to 0.76 at 3*g*. Hence, at 3*g*
544 the systolic phase becomes predominant over diastole, resulting in the
545 aforementioned drop of the SV_{dia}/SV_{sys} ratio.

In figure 5, the mean values and amplitudes (computed as the difference between maximum and minimum values) of the central aortic pressure (P_{aa}), central venous pressure (CVP), pulmonary artery pressure (P_{pa}), and pulmonary capillary wedge pressure ($PCWP$) are displayed as function of the gravitational acceleration. These pressures provide crucial information regarding the overall hemodynamic status of the heart. In fact, P_{aa} and P_{pa} represent the pressure level at the left and right ventricular outlets, whereas CVP and $PCWP$ reflect the pressure within the right and left atria, respectively.

Figure 5a shows how mean and pulsatile values within the aortic root ($\overline{P_{aa}}$ and ΔP_{aa}, respectively) vary with g. Specifically, $\overline{P_{aa}}$ initially increases with g, varying from 92 mmHg at 0g to 96.2 mmHg at 1g. This slight increase is due to the inotropic effect and the heightened peripheral vascular resistance triggered by short-term regulation mechanisms. $\overline{P_{aa}}$ is nearly constant up to 2g, maintaining a value close to 96 mmHg, whereas at 3g a moderate decrease is detected, with $\overline{P_{aa}}$ reaching 92 mmHg. Due to the almost opposite behaviour of DAP and SAP, ΔP_{aa} decreases with rising g, reducing from 51.7 mmHg at 0g to 23.0 mmHg at 3g (-55.5%). This decline in ΔP_{aa} reflects the drop in the left ventricle SV, confirming the close relationship between these two hemodynamic parameters (Hall & Hall, 2020).

CVP, mean pulmonary arterial pressure ($\overline{P_{pa}}$) and $PCWP$ (Fig. 5b, 5c and 5d) are significantly affected by gravity acceleration and, contrary to $\overline{P_{aa}}$, exhibit a (non-linear) decreasing trend with increasing g. These pressures are characterized by much lower values than central aortic pressure and, therefore, are more susceptible to changes in intrathoracic pressure (ITP). Specifically,

571 at higher g values the diaphragm is pulled towards the abdominal cavity,
572 leading to a reduction in *ITP* (Videbaek & Norsk, 1997; Peterson *et al.*, 2002).
573 Hence, the mean values of *CVP* and *PCWP* follow a similar decreasing
574 behaviour, reducing from 6.6 mmHg to -1 mmHg (-115% from 0g to 3g) and
575 from 8.1 mmHg to 0.5 mmHg (-94% from 0g to 3g), respectively. With
576 regards to pulsatile values of the pressure within the right and left atria, both
577 decrease with rising g, as a result of the progressively reduced venous return
578 and the subsequent decrease in atrial filling elicited by the increasing
579 gravitational force. Similarly, both the mean and pulsatile values of P_{pa} exhibit
580 a monotonic decline, diminishing from 15.4 mmHg to 5.5 mmHg (-64.3%
581 from 0g to 3g) and from 13.9 mmHg to 6.3 mmHg (-54.7% from 0g to 3g),
582 respectively. Notably, the trends observed for $\overline{P_{pa}}$, $\overline{CVP}$ and $\overline{PWCP}$ decrease
583 non-linearly with g. In particular, most of the drop occurs within the gravity
584 range [0g-2g], with minor variations in the upper region of the investigated
585 hyper-gravity range.
586

Table 1. Key findings of the cardiac function in micro- ([0*g*-1*g*]) and hyper-gravity ([1*g*-3*g*]). Legend: ≈: not clear trend; ≈↑ or ≈↓: slight increase or decrease; ↑ or ↓: increase or decrease; ↑↑ or ↓↓ great increase or decrease.

Hemodynamic parameters		**[0*g*-1*g*]**		**[1*g*-3*g*]**	
Left heart	**mechano-energetic**	*PV* loop	shifts and stretches horizontally	*PV* loop	shifts and shrinks horizontally
		EW/min	≈↑ (+6%)	*EW/min*	↓ (-22.6%)
		PVA/min	≈ (+0.8%)	*PVA/min*	↓ (-15.7%)
	oxygen consumption	*RPP*	↓ (-15.9%)	*RPP*	↑↑ (+41.8%)
		TTI/min	≈ (-0.3%)	*TTI/min*	≈↑ (+6.8%)
	efficiency	*EF*	↑ (+9.9%)	*EF*	↓ (-15.3%)
		LVE	≈↑ (+5.3%)	*LVE*	≈↓ (-8.1%)
Right heart	**mechano-energetic**	*PV* loop	shifts and stretches vertically and horizontally	*PV* loop	shifts and shrinks vertically and horizontally
		EW/min	↑ (+26.0%)	*EW/min*	↓↓ (-33.5%)
		PVA/min	↑ (+25.5%)	*PVA/min*	↓↓ (-32.9%)
	efficiency	*EF*	≈↑ (+4.2%)	*EF*	↓ (-12.3%)
		RVE	≈ (+0.6%)	*RVE*	≈ (-0.9%)
Coronary perfusion		*SV*	↑	*SV*	↓
		CBF	↓	*CBF*	↑
		CPP	↓	*CPP*	↑
		Amplitude and shape changes of Q_{LAD} signals as g increases from 0g to 3g			
Central pressures	**Mean values**	P_{aa}	≈	P_{aa}	≈
		P_{pa}	↑	P_{pa}	↓
		CVP	↑	*CVP*	↓
		PCWP	↑	*PCWP*	↓
	Amplitude	P_{aa}	↑	P_{aa}	↓↓
		P_{pa}	↑	P_{pa}	↓↓
		CVP	≈↑	*CVP*	↓↓
		PCWP	↑	*PCWP*	↓↓

5. Discussion

The existing literature on cardiac function under altered gravity conditions appears rather fragmented and characterized by several sources of uncertainty. The limited number of studies, the challenges in acquiring clinical measures in difficult conditions, and the significant inter- and intra-study differences restrict the knowledge of the cardiovascular response to a small set of hemodynamic parameters (Blaber *et al.*, 2010; Zhu *et al.*, 2015; Hughson *et al.*, 2018; Shen & Frishman, 2019; Norsk, 2020; Goswami *et al.*, 2021). As a result, information is lacking regarding several key aspects of cardiac behaviour, such as energy performance, oxygen consumption, right heart function, and coronary perfusion at different levels of gravitational force. In order to shed light on these gaps, in this work, we have exploited our mathematical framework to provide novel insights into the left and right cardiac hemodynamics within the gravity range [0*g*-3*g*].

Results indicate that transitions from micro- to hyper-gravity elicit different responses between left and right heart hemodynamics. Within the hypo-gravity range (i.e., [0*g*-1*g*]), the venous return is increased due to fluid shift from the caudal to the cranial region. Consequently, in micro-gravity, both the left and right ventricular chambers receive a larger quantity of blood, with both end-systolic and end-diastolic volumes increasing as gravity approaches 0*g*, resulting in an increased ventricular preload. However, as depicted in figure 3, the left ventricular *PV* loop exhibits a horizontal shift, whereas in the right ventricle, both horizontal and vertical shifts are detected, as both end-systolic and end-diastolic pressures increase when entering the hypo-gravity range. This different behaviour between left and right ventricles

615 was already observed by Gerber et al. (2018), who suggested that an increase
616 in *CVP* is responsible for this right ventricular *PV* loop upward shift.
617 Coherently with this observation, our cardiovascular model predicts an
618 increase in *CVP* (from 1.8 mmHg at 1*g* to 6.6 mmHg at 0*g*) during short-term
619 micro-gravity exposure in standing posture. However, actual spaceflight data
620 on *CVP* reveal some discrepancies. For instance, Buckey et al. (1996) reported
621 a decrease in *CVP* during micro-gravity with respect to supine and seated pre-
622 flight values, whereas Foldager et al. (1996) detected an increase in *CVP* both
623 in seated and standing postures. In addition to the rise in *CVP*, the upward
624 shift of the right ventricular *PV* loop could be explained by a reduced activity
625 of short-term regulation mechanisms for the cardiopulmonary circulation,
626 such as the baroreceptors and cardiopulmonary reflex. In systemic circulation,
627 these mechanisms regulate total peripheral resistance to maintain adequate
628 arterial pressure across a wide range of gravitational acceleration (see Fig 5a).
629 On the contrary, the total resistance of the pulmonary circulation is governed
630 by other factors, such as respiratory gasses, humoral and neural mechanisms
631 (Barnes & Liu, 1995). Our mathematical model does not implement these
632 mechanisms, resulting in a constant pulmonary vascular resistance throughout
633 the entire gravity range. Consequently, the micro-gravity-induced increase in
634 stroke volume and cardiac output leads to elevated right ventricle end-systolic
635 and diastolic pressures. As a result, the right ventricle *PV* loop is more affected
636 by gravity variations than its left counterpart. This is also evident from the
637 analysis of the mechano-energetic parameters. Specifically, as gravity varies
638 from 1*g* to 0*g*, *EW/min* increases by +6% in the left ventricle (from 71.6 J/min
639 at 1*g* to 76.1 J/min at 0*g*) and by +26% in the right ventricle (from 9.4 J/min

at 1*g* to 11.8 J/min at 0*g*), respectively. Moreover, *PVA/min*, which represents the total mechanical energy produced by ventricular contraction, is almost constant for the left ventricle (+0.8% from 1*g* to 0*g*), whereas an increase of +25.5% is detected in PVA_{rv}/min. Additionally, together with a rise in the mechano-energetic indexes, a reduction in oxygen consumption parameters (i.e., *RPP* and *TTI/min*) and an increase in cardiac efficiency (i.e., $EF_{lv/rv}$, *LVE* and *RVE*) are observed, suggesting that cardiac performance is enhanced during short-term exposure to micro-gravity.

In the hyper-gravity range (i.e., [1*g*-3*g*]), a reduction in both *PV* loop widths is observed (see Fig. 3a and Fig. 3b), affecting both *SV* and left/right cardiac performance. Due to the above-mentioned different response between left and right ventricles, the right *PV* loop also shrinks in the vertical direction. However, contrary to micro-gravity, short-term exposure to hyper-gravity elicits a significant decrease in both the left and right *EW/min*: EW_{lv}/min decreases by -22.6% and EW_{rv}/min diminishes by -33.5% as *g* rises from 1*g* to 3*g*. Since *EW/min* is a proxy of cardiac energy supply (Westerhof *et al.*, 2019; Koeppen & Stanton, 2023), its decrease indicates a loss of cardiac performance, which no longer appears sufficient during hyper-gravity exposure. In this context, our model outputs show that an increase in *g* is associated with an increment in oxygen consumption indexes *RPP* and *TTI/min*. In particular, *RPP* increases by +41.8% as gravitational force varies from 1*g* to 3*g*. This indicates that the cardiac energy demand in hyper-gravity is notably increased. Consequently, taking into account the simultaneous drop in *EW/min*, our simulations suggest an imbalance between the energy demand and supply within the hyper-gravity range. Impairment of cardiac performance

665 is further supported by the behaviour of the ventricular efficiency indexes:
666 LVE, EF_{lv} and EF_{rv} decrease monotonically with increasing g, while RVE is
667 nearly constant. Specifically, at 3g, both ejection fractions fall below 50%.
668 This value is critical, being EF values between 40% and 49% associated with
669 heart failure with mildly reduced ejection fraction (Savarese *et al.*, 2022).
670 The hyper-gravity scenario is further complicated by an impairment
671 between myocardial oxygen demand and coronary perfusion. Specifically, the
672 increase in HR, induced by the baroreflex, elicits an altered RR_{sys}/RR_{dia} ratio,
673 increasing the systolic phase over the diastolic duration. This results in a
674 $SV_{LAD/RCA}$ reduction, which is only partially mitigated by HR. In fact, both
675 CBF_{LAD} and CBF_{RCA} increase non-linearly, exhibiting a downward concavity
676 and reaching a maximum in the proximity of 2.8 g. Hence, at higher g values
677 the increase in CBF is slowed down, failing to compensate for the larger rise
678 in RPP, thus producing an energy mismatch even at the coronary level. Similar
679 findings have been observed in studies of coronary circulation during
680 arrhythmias at varying heart rates (Scarsoglio *et al.*, 2019; Gamilov *et al.*,
681 2020). Additionally, our numerical model allowed us to analyze the flow rate
682 waveform in the left ascending coronary artery, highlighting both amplitude
683 and shape distortions of Q_{LAD} signals as g increases from 0g to 3g.
684 One of the advantages of our mathematical framework is that it allows
685 for a direct investigation of mean and pulsatile values of the pressure signal in
686 regions of the cardiovascular system that are challenging to access using
687 current measurement methods. In this context, we evaluated the behaviour of
688 mean and pulsatile values of the pressure at the initial and final sites of the
689 systemic (P_{aa} and CVP) and cardiopulmonary (P_{pa} and $PCWP$) circulations,

690 respectively. The cardiovascular model highlights a different behaviour
691 between the mean values of P_{aa} and the mean values of CVP, P_{pa} and $PCWP$.
692 The latter (CVP, P_{pa} and $PCWP$) are more susceptible to changes in
693 intrathoracic pressure with respect to aortic pressure, which, instead, remains
694 stable across the entire range of gravitational acceleration. Additionally, the
695 absence of a regulation mechanism similar to that of the baroreceptors
696 contributes to the decline in P_{pa} mean values as g increases. Consequently, the
697 driving pressures of the systemic ($P_{aa} - CVP$) and cardiopulmonary ($P_{pa} -$
698 $PCWP$) circulations respond differently: at 3g with respect to 0g, the driving
699 pressure varies by +13% in the systemic circulation and by -30% in the
700 cardiopulmonary circulation. Conversely, the pulsatility of these pressures
701 exhibits similar behaviour with g variation. Specifically, an increment in all
702 the pulsatilities is observed in the hypo-gravity range (from 1g to 0g: +28.0%
703 for ΔP_{aa}, +28.8% for ΔP_{pa}, +8.7 for ΔCVP, and +26.8 for $\Delta PCWP$), whereas
704 the exact opposite is detected in the hyper-gravity range (from 1g to 3g: -
705 43.2% for ΔP_{aa}, -41.9\% for ΔP_{pa}, -42.3 for ΔCVP, and -42.6 for $\Delta PCWP$).
706 This behaviour is due to the strong association between the stroke volume and
707 pressure pulsatility (Hall & Hall, 2020).

708 The present mathematical framework has some limiting aspects.
709 Specifically, each model parameter has a degree of uncertainty, which is
710 challenging to quantify due to the high inter-subject variability. These
711 parameters are influenced by several factors, including the subject's sex,
712 anthropometric features and age. In this context, future studies could
713 investigate how some parameters affect the cardiac response to gravity
714 changes, addressing important physiological and medical issues such as

arterial ageing, individual variability for subject-specific applications, and gender differences. In addition, our model does not account for muscular activation – which may play an important role in venous return to the heart, especially during hyper-gravity exposure – and neglects the influence of tissue weight. The implemented regulation mechanisms are limited to the baroreceptors and the cardiopulmonary reflexes, thus neglecting other mechanisms, such as metabolic regulation and reactivity to CO_2 and O_2 concentrations. Furthermore, in our model, the pulmonary vascular resistance is assumed to be constant, whereas it is known to be non-linear and dependent on active (respiratory gasses, humoral and neural mechanisms) and passive factors (cardiac output, left atrial pressure, airway and interstitial pressure) (Barnes & Liu, 1995). Finally, long-term regulation mechanisms related to renal, hormonal activity and transcapillary blood flow are not described. The reduction (even partial) of these limitations will be needed for future studies aiming to investigate the long-term cardiovascular response.

6. Conclusions

The cardiovascular model described in this study provided valuable insights into cardiac function under micro- and hyper-gravity conditions, demonstrating to be a valid approach for investigating hemodynamic parameters which are challenging to measure directly using current acquisition methodologies. To the authors' knowledge, for the first time, the cardiac response across the entire spectrum from micro- to hyper-gravity is described in depth, and some crucial aspects emerge clearly. Firstly, the different behaviour between the left and right hearts, with the latter being more susceptible to gravity changes in terms of pressure and energy supply

(*EW/min*). Secondly, our findings indicated that, in the short-term, micro-gravity exerted less stress on the heart due to enhanced venous return and ventricular filling, leading to improved cardiac energy performance and efficiency. Conversely, hyper-gravity imposed more stress on the cardiovascular system, leading to an energy supply/demand imbalance at both the cardiac and coronary levels. In particular, within the coronary circulation, the increase in *HR* at higher *g* values was insufficient to compensate for the reduction in coronary stroke volume, which occurred due to the reduced RR_{dia}/RR_{sys} ratio. Finally, our study highlighted that gravity significantly affected both mean and pulsatile values of central pressures, with increased pulsatility in micro-gravity and reduced pulsatility in hyper-gravity.

The picture of cardiac behaviour under gravitational stress outlined in this work opens the way to the study of the consequences that it has on other body districts. In this regard, it is sufficient to mention that higher pulsatility at the central level is typically associated with elevated variability in both cerebral blood flow and intracranial pressure (Scarsoglio *et al.*, 2023). Since alterations in *CBF* and *ICP*, along with variations in intraocular pressure, are implicated in the onset of SANS, it follows that gravity-induced alteration of the cardiac response plays a crucial role in one of the most serious pathologies that can affect astronauts.

Our work demonstrates that mathematical modeling can usefully complement the usual clinical and experimental approaches, helping to shed light on currently unclear physiological and pathological mechanisms, with the aim of identifying effective countermeasures to be adopted in space flights.

Additional information

Data availability statement

All model equations, parameter settings, code and generated raw simulation data are available on Figshare, along with the experimental data used for model validation (https://doi.org/10.6084/m9.figshare.29064842).

Competing interests

The authors declare that they have no competing interests that could have appeared to influence the work reported in this paper.

Author contributions

F.T., L.R., and S.S. conceived and designed the research, analyzed and interpreted the results, edited, and revised the manuscript. F.T. performed the numerical simulations. F.T. drafted the manuscript and prepared the figures. All authors reviewed and approved the final version of the manuscript.

Funding

This study was carried out within the I-2022-05387 "Optimizing countermeasures against cardiovascular deconditioning and cerebral hemodynamics changes in long-term human spaceflights" project, which was selected via the Open Space Innovation Platform (https://ideas.esa.int) as a Co-Sponsored Research Agreement and carried out under the Discovery programme of, and funded by, the European Space Agency (contract number: 4000141523). This manuscript reflects only the authors' views and opinions and the European Space Agency cannot be considered responsible for them.

Figures

Figure 1. Schematic representation of the closed-loop 0D-1D multiscale model of the cardiovascular system. On the left, the 1D arterial tree is depicted in red, with numbers, and yellow and green circles indicating the specific arterial vessel, the outlets and the inlet of the 1D arterial tree, respectively. On the right, a representation of the 0D peripheral circulation, which is organized into five body regions (extracranial circulation, arms, upper abdomen, lower abdomen, and legs), is shown. Vertical rectangles refer to arteriolar, capillary, venular, venous and venae cavae compartments. The *k-th* generic 0D coronary microvascular district is depicted in the left box, the boxes on the right represent the cardio-pulmonary circulation, whereas the grey box at the bottom shows the *j-th* generic 0D compartment Q_j is the flow rate, p_j is the pressure, Δp_j^h is the hydrostatic gradient, and R_j, C_j and L_j are compartmental resistance, compliance and inertance, respectively).

Figure 2. Pooled mean μ^p_{Xj} and standard deviation σ^p_{Xj}, for the *X-th* cardiac parameter at gravity level *j*, are reported with vertical red (centrifuges data), blue (parabolic flights data in standing posture), and yellow (parabolic flights data in sitting posture) points and lines. The model outcomes are depicted with black solid curves, whereas the dashed curves represent the regression lines computed using the weighted least-squares fitting method. Trends in *SV* (p-value < 0.001), *HR* (p-value < 0.001), *MAP* (p-value < 0.001), *SAP* (p-value = 0.0161) and *DAP* (p-value < 0.001) are statistically significant, whereas *CO* fails to pass the t-test with a p-value equal to 0.130.

Figure 3. Left and right columns report *PV* loops (panels a and b), mechano-energetics (panels c and d), efficiency (panels e and f) and oxygen consumption parameters (panel g) for left and right ventricles, respectively.

Figure 4. Coronary blood flow and coronary perfusion parameters: panel a) shows the coronary stroke volume in the LAD (SV_{LAD}) and RCA (SV_{RCA}) along with the SV_{LAD}/SV_{RCA} ratio; panels b) and c) show the *SV* partition between diastolic and systolic phases; panels d) and e) illustrate the coronary blood flow (*CBF*) and the coronary perfusion pressure (*CPP*), respectively; panels f), g) and h) show the impact of gravity changes on Q_{LAD} waveform.

Figure 5. Mean values (solid lines) and amplitudes (shaded area) of: a) ascending aortic pressure; b) central venous pressure; c) pulmonary artery pressure; and d) pulmonary capillary wedge pressure.

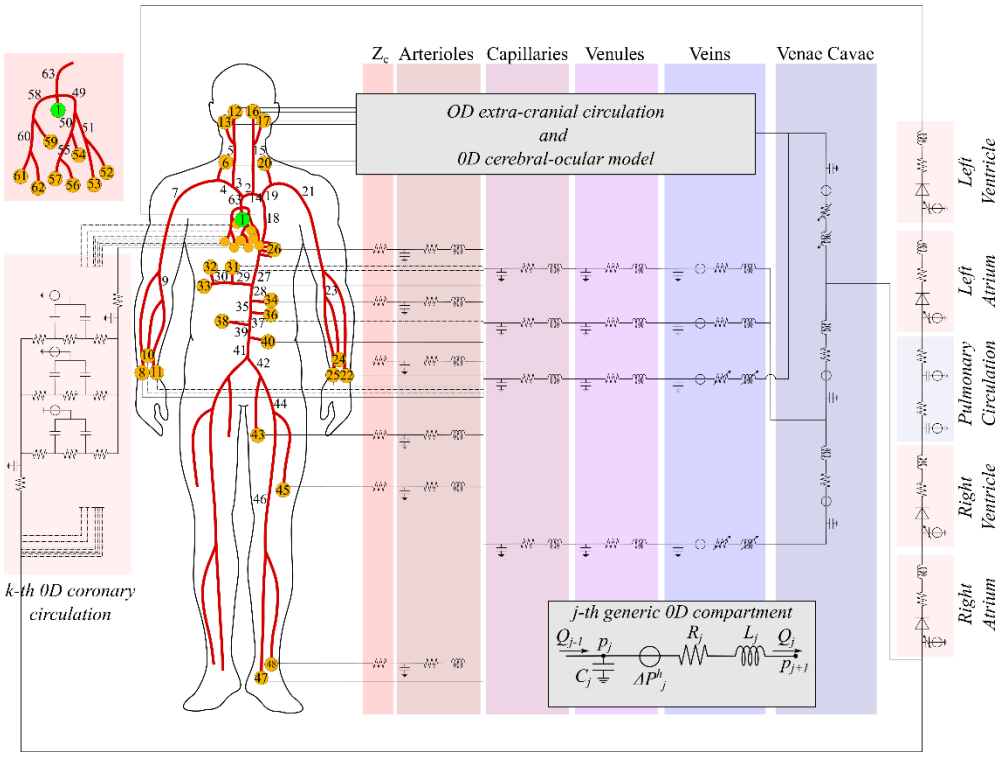
Zc
Arterioles
Capillaries
Venules
Veins
Venae Cavae
OD extra-cranial circulation
and
0D cerebral-ocular model
Left Ventricle
Left Atrium
Pulmonary Circulation
Right Ventricle
Right Atrium
k-th 0D coronary circulation
j-th generic 0D compartment

822

823

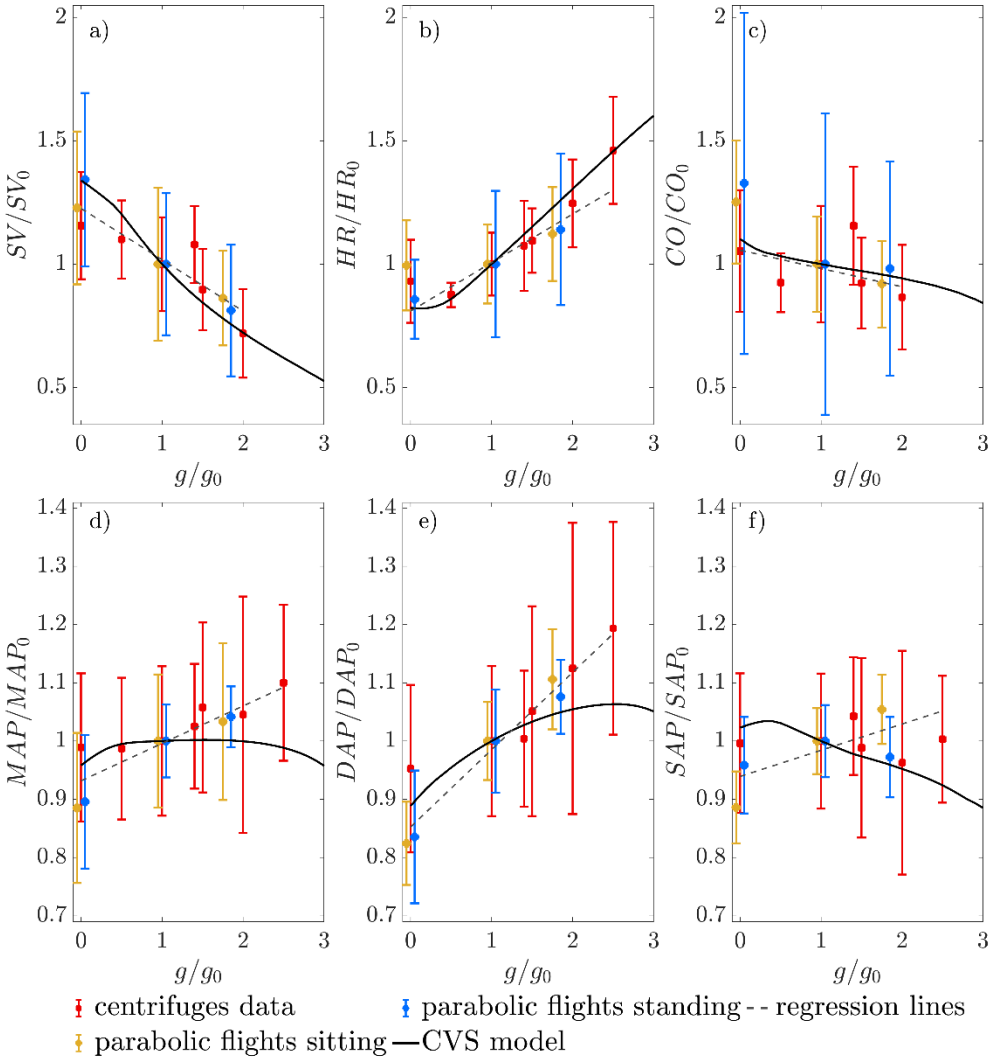
a)
b)
c)
d)
e)
f)
SV/SV_0
HR/HR_0
CO/CO_0
MAP/MAP_0
DAP/DAP_0
SAP/SAP_0
g/g_0
centrifuges data
parabolic flights standing
regression lines
parabolic flights sitting
CVS model

824

825

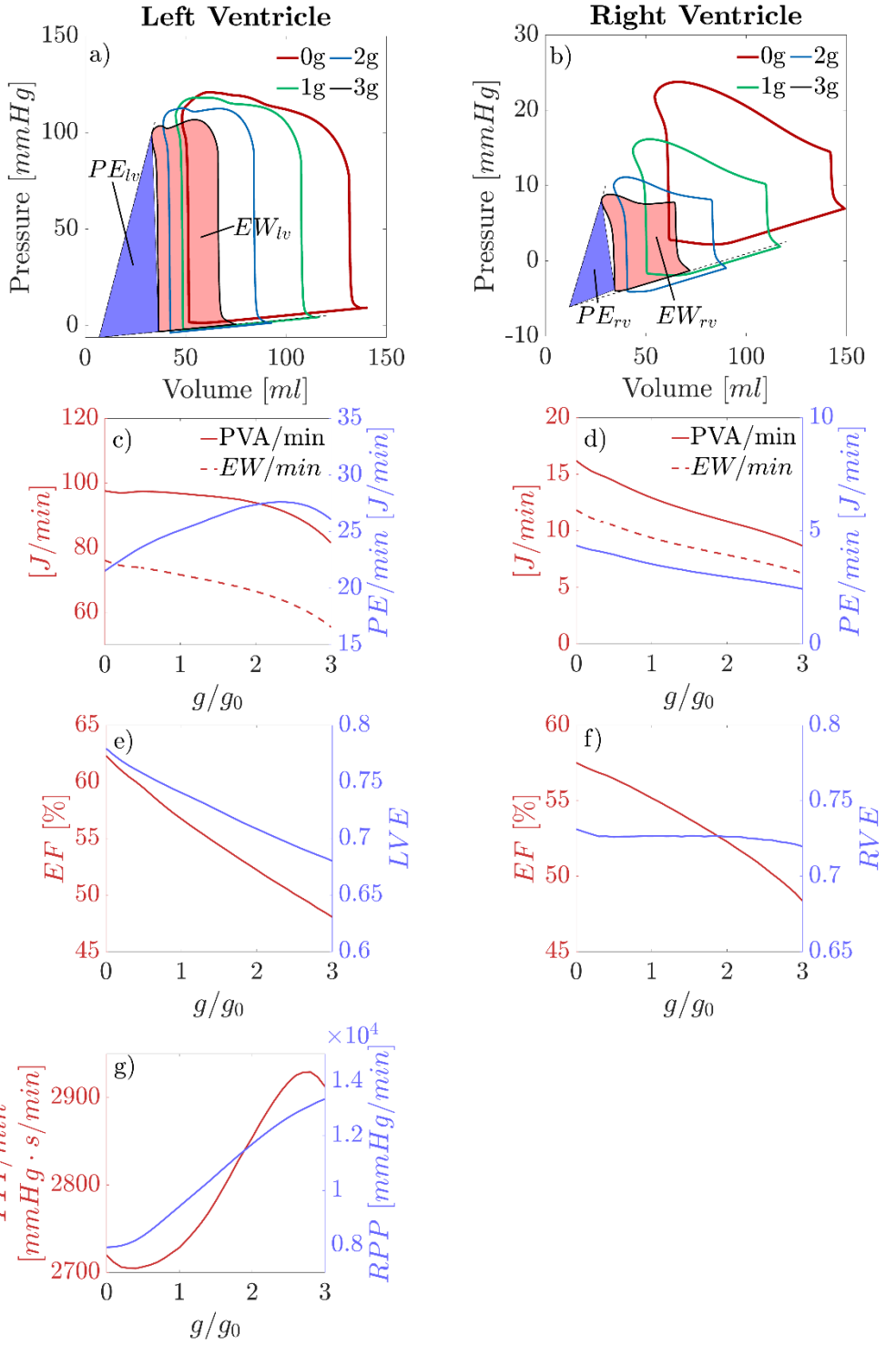
Left Ventricle
Right Ventricle
a)
b)
c)
d)
e)
f)
g)
0g
2g
1g
3g
Pressure [mmHg]
Volume [ml]
PE_{lv}
EW_{lv}
PE_{rv}
EW_{rv}
PVA/min
EW/min
[J/min]
PE/min [J/min]
g/g_0
EF [%]
LVE
RVE
TTI/min [mmHg · s/min]
RPP [mmHg/min]
$\times 10^4$

826

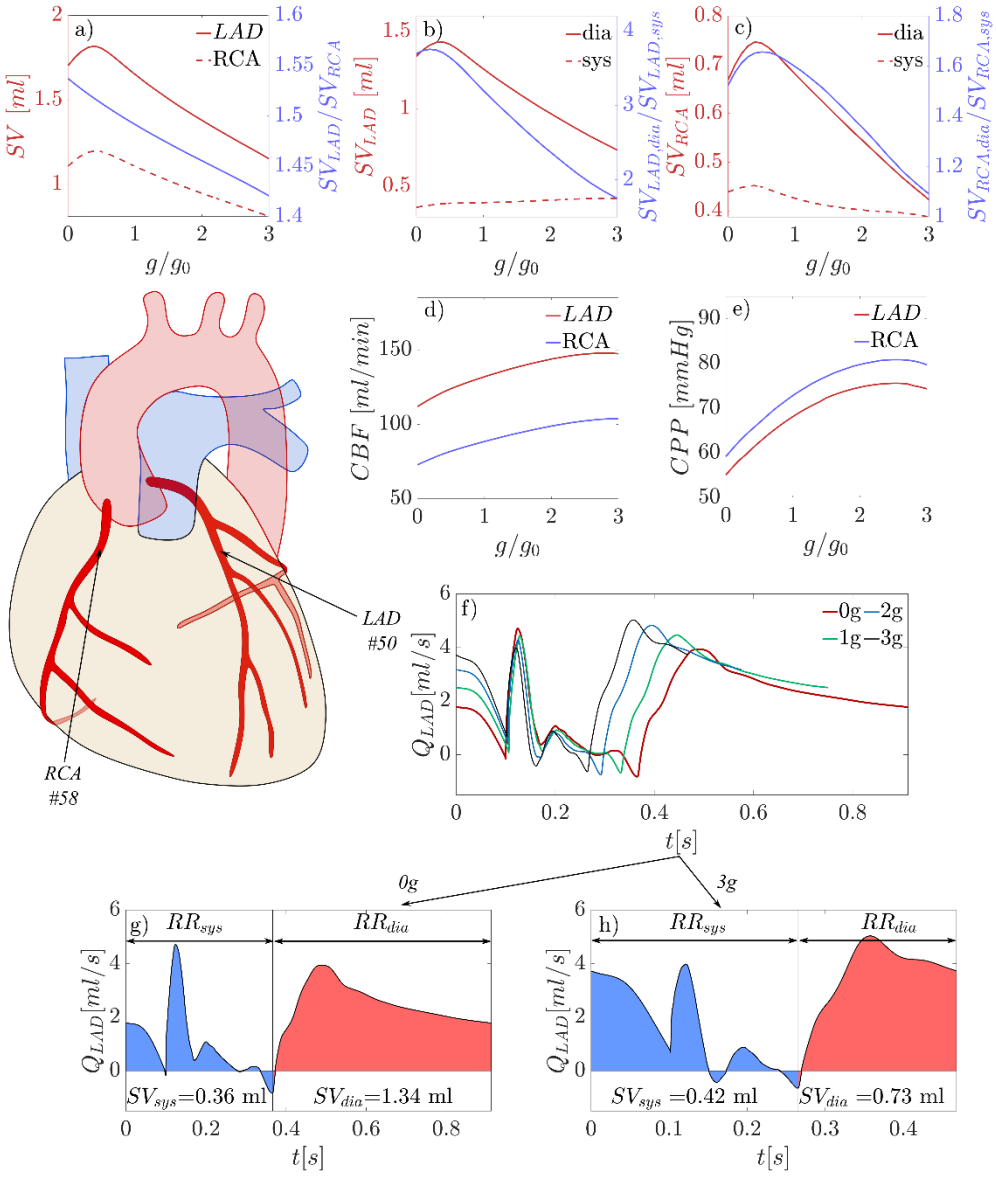
a)
LAD
RCA
SV [ml]
SV_{LAD}/SV_{RCA}
g/g0
b)
dia
sys
SV_{LAD} [ml]
$SV_{LAD,dia}/SV_{LAD,sys}$
c)
SV_{RCA} [ml]
$SV_{RCA,dia}/SV_{RCA,sys}$
d)
CBF [ml/min]
e)
CPP [mmHg]
LAD #50
RCA #58
f)
0g 2g
1g 3g
Q_{LAD}[ml/s]
t[s]
0g
3g
g) RR_{sys} RR_{dia}
SV_{sys}=0.36 ml
SV_{dia}=1.34 ml
h) RR_{sys} RR_{dia}
SV_{sys} =0.42 ml
SV_{dia} =0.73 ml

827

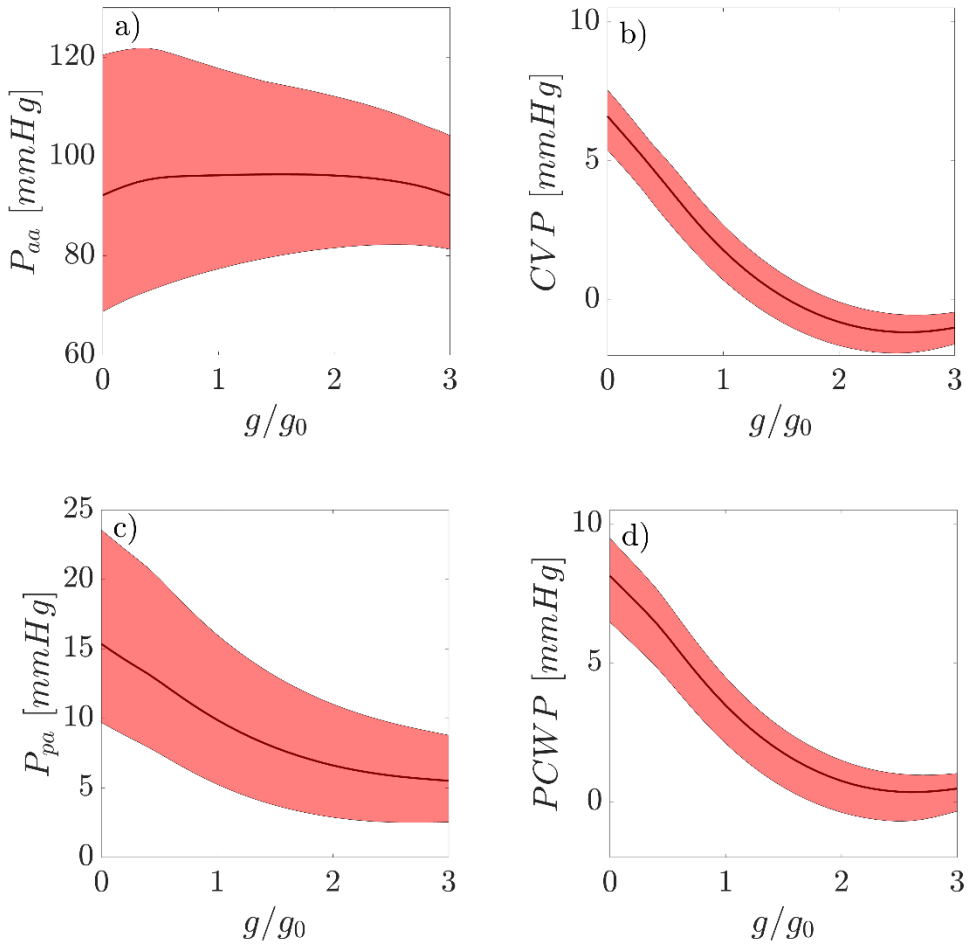
a)
120
100
80
60
P_{aa} [$mmHg$]
0
1
2
3
g/g_0
b)
10
5
0
CVP [$mmHg$]
0
1
2
3
g/g_0
c)
25
20
15
10
5
0
P_{pa} [$mmHg$]
0
1
2
3
g/g_0
d)
10
5
0
$PCWP$ [$mmHg$]
0
1
2
3
g/g_0

828

References

Anselmino M, Scarsoglio S, Saglietto A, Gaita F & Ridolfi L (2016). Transient cerebral hypoperfusion and hypertensive events during atrial fibrillation: a plausible mechanism for cognitive impairment. *Sci Rep* **6,** 28635.

Arbeille P, Fomina G, Roumy J, Alferova I, Tobal N & Herault S (2001). Adaptation of the left heart, cerebral and femoral arteries, and jugular and femoral veins during short- and long-term head-down tilt and spaceflights. *Eur J Appl Physiol* **86,** 157–168.

Barnes PJ & Liu SF (1995). Regulation of pulmonary vascular tone. *Pharmacol Rev* **47,** 87–131.

Beckers F, Seps B, Ramaekers D, Verheyden B & Aubert AE (2003). Parasympathetic heart rate modulation during parabolic flights. *Eur J Appl Physiol* **90,** 83–91.

Berdahl JP, Yu DY & Morgan WH (2012). The translaminar pressure gradient in sustained zero gravity, idiopathic intracranial hypertension, and glaucoma. *Med Hypotheses* **79,** 719–724.

Blaber E, Marçal H & Burns BP (2010). Bioastronautics: The Influence of Microgravity on Astronaut Health. *Astrobiology* **10,** 463–473.

Blomqvist CG & Stone HL (1983). Cardiovascular Adjustments to Gravitational Stress. *Compr Physiol*1025–1063.

Borenstein M, Hedges L V., Higgins JPT & Rothstein HR (2009). *Introduction to Meta-Analysis*. Wiley. Available at: https://onlinelibrary.wiley.com/doi/book/10.1002/9780470743386.

Buckey JC (2006). *Space Physiology*. Oxford University PressNew York, NY.

Buckey JC, Gaffney FA, Lane LD, Levine BD, Watenpaugh DE, Wright SJ, Yancy CW, Meyer DM & Blomqvist CG (1996). Central venous pressure in space. *J Appl Physiol* **81,** 19–25.

Burton RR (1988). A human-use centrifuge for space stations: Proposed ground-based studies. *Aviat Space Environ Med* **59,** 579–582.

Caiani EG, Sugeng L, Weinert L, Capderou A, Lang RM & Vaïda P (2006). Objective evaluation of changes in left ventricular and atrial volumes during parabolic flight using real-time three-dimensional echocardiography. *J Appl Physiol* **101,** 460–468.

Caiani EG, Weinert L, Takeuchi M, Veronesi F, Sugeng L, Corsi C, Capderou A, Cerutti S, Vaïda P & Lang RM (2007). Evaluation of alterations on mitral annulus velocities, strain, and strain rates due to abrupt changes in preload elicited by parabolic flight. *J Appl Physiol* **103,** 80–87.

Canuto D, Chong K, Bowles C, Dutson EP, Eldredge JD & Benharash P (2018). A regulated multiscale closed-loop cardiovascular model, with applications to hemorrhage and hypertension. *Int J Numer Method Biomed Eng* **34,** e2975.

Clément G (2011). *Fundamentals of Space Medicine*. Springer New York.

Clément GR, Bukley AP & Paloski WH (2015). Artificial gravity as a countermeasure for mitigating physiological deconditioning during long-duration space missions. *Front Syst Neurosci* **9,** 92.

Convertino VA (1998). High sustained +Gz acceleration: physiological adaptation to high-G tolerance. *J Gravit Physiol* **5,** P51-4.

877 Diaz-Artiles A, Heldt T & Young LR (2018). Short-Term Cardiovascular
878 Response to Short-Radius Centrifugation With and Without Ergometer
879 Exercise. *Front Physiol*; DOI: 10.3389/fphys.2018.01492.
880 Diaz-Artiles A, Heldt T & Young LR (2019). Computational model of
881 cardiovascular response to centrifugation and lower body cycling
882 exercise. *J Appl Physiol* **127,** 1453–1468.
883 Fois M, Diaz-Artiles A, Zaman SY, Ridolfi L & Scarsoglio S (2024). Linking
884 cerebral hemodynamics and ocular microgravity-induced alterations
885 through an in silico-in vivo head-down tilt framework. *NPJ Microgravity*
886 **10,** 22.
887 Fois M, Maule SV, Giudici M, Valente M, Ridolfi L & Scarsoglio S (2022*a*).
888 Cardiovascular Response to Posture Changes: Multiscale Modeling and
889 in vivo Validation During Head-Up Tilt. *Front Physiol* **13,** 826989.
890 Fois M, Ridolfi L & Scarsoglio S (2022*b*). In silico study of the posture-
891 dependent cardiovascular performance during parabolic flights. *Acta*
892 *Astronaut* **200,** 435–447.
893 Foldager N, Andersen TA, Jessen FB, Ellegaard P, Stadeager C, Videbaek R
894 & Norsk P (1996). Central venous pressure in humans during
895 microgravity. *J Appl Physiol* **81,** 408–412.
896 Fontolliet T, Pichot V, Antonutto G, Bonjour J, Capelli C, Tam E, Barthélémy
897 J-C & Ferretti G (2015). Effects of gravitational acceleration on
898 cardiovascular autonomic control in resting humans. *Eur J Appl Physiol*
899 **115,** 1417–1427.

900 Gallo C, Ridolfi L & Scarsoglio S (2020). Cardiovascular deconditioning
901 during long-term spaceflight through multiscale modeling. *NPJ*
902 *Microgravity* **6,** 27.
903 Gamilov T, Kopylov P, Serova M, Syunyaev R, Pikunov A, Belova S, Liang
904 F, Alastruey J & Simakov S (2020). Computational Analysis of Coronary
905 Blood Flow: The Role of Asynchronous Pacing and Arrhythmias.
906 *Mathematics* **8,** 1205.
907 Gerber B, Singh J-L, Zhang Y & Liou W (2018). A computer simulation of
908 short-term adaptations of cardiovascular hemodynamics in microgravity.
909 *Comput Biol Med* **102,** 86–94.
910 Goswami N, Bruner M, Xu D, Bareille M-P, Beck A, Hinghofer-Szalkay H &
911 Blaber AP (2015). Short-arm human centrifugation with 0.4g at eye and
912 0.75g at heart level provides similar cerebrovascular and cardiovascular
913 responses to standing. *Eur J Appl Physiol* **115,** 1569–1575.
914 Goswami N, White O, Blaber A, Evans J, van Loon JJWA & Clement G
915 (2021). Human physiology adaptation to altered gravity environments.
916 *Acta Astronaut* **189,** 216–221.
917 Grigoriev AI, Kotovskaya AR & Fomina GA (2011). The human
918 cardiovascular system during space flight. *Acta Astronaut* **68,** 1495–
919 1500.
920 Habazettl H, Stahn A, Nitsche A, Nordine M, Pries AR, Gunga H-C & Opatz
921 O (2016). Microvascular responses to (hyper-)gravitational stress by
922 short-arm human centrifuge: arteriolar vasoconstriction and venous
923 pooling. *Eur J Appl Physiol* **116,** 57–65.

Hall JE & Hall ME (2020). *Guyton and Hall Textbook of Medical Physiology E-Book: Guyton and Hall Textbook of Medical Physiology E-Book*. Elsevier Health Sciences.

Hargens AR, Bhattacharya R & Schneider SM (2013). Space physiology VI: exercise, artificial gravity, and countermeasure development for prolonged space flight. *Eur J Appl Physiol* **113,** 2183–2192.

Hargens AR & Richardson S (2009). Cardiovascular adaptations, fluid shifts, and countermeasures related to space flight. *Respir Physiol Neurobiol* **169,** S30–S33.

Heldt T, Shim EB, Kamm RD & Mark RG (2002). Computational modeling of cardiovascular response to orthostatic stress. *J Appl Physiol* **92,** 1239–1254.

Holmlund P, Eklund A, Koskinen L-OD, Johansson E, Sundström N, Malm J & Qvarlander S (2018). Venous collapse regulates intracranial pressure in upright body positions. *American Journal of Physiology-Regulatory, Integrative and Comparative Physiology* **314,** R377–R385.

Hughson RL, Helm A & Durante M (2018). Heart in space: effect of the extraterrestrial environment on the cardiovascular system. *Nat Rev Cardiol* **15,** 167–180.

Karmali F & Shelhamer M (2008). The dynamics of parabolic flight: Flight characteristics and passenger percepts. *Acta Astronaut* **63,** 594–602.

Klein T, Wollseiffen P, Sanders M, Claassen J, Carnahan H, Abeln V, Vogt T, Strüder HK & Schneider S (2019). The influence of microgravity on cerebral blood flow and electrocortical activity. *Exp Brain Res* **237,** 1057–1062.

949 Koeppen BM & Stanton BA (2023). *Berne and Levy Physiology E-Book:*
950 *Berne and Levy Physiology E-Book*, 8th edn.ed. Hall JM & Swiatecka-
951 Urban A. Elsevier Health Sciences. Available at:
952 https://shop.elsevier.com/books/berne-and-levy-physiology/hall/978-0-
953 323-84790-2 [Accessed April 15, 2025].
954 Konishi T, Kurazumi T, Kato T, Takko C, Ogawa Y & Iwasaki K (2019).
955 Changes in cerebral oxygen saturation and cerebral blood flow velocity
956 under mild +Gz hypergravity. *J Appl Physiol* **127,** 190–197.
957 Lalande S & Buick F (2009). Physiologic +Gz Tolerance Responses Over
958 Successive +Gz Exposures in Simulated Air Combat Maneuvers. *Aviat*
959 *Space Environ Med* **80,** 1032–1038.
960 Lathers CM, Charles JB, Elton KF, Holt TA, Mukai C, Bennett BS & Bungo
961 MW (1989). Acute Hemodynamic Responses to Weightlessness in
962 Humans. *The Journal of Clinical Pharmacology* **29,** 615–627.
963 Liu J, Verheyden B, Beckers F & Aubert AE (2012). Haemodynamic
964 adaptation during sudden gravity transitions. *Eur J Appl Physiol* **112,** 79–
965 89.
966 Lu K, Clark JW, Ghorbel FH, Ware DL & Bidani A (2001). A human
967 cardiopulmonary system model applied to the analysis of the Valsalva
968 maneuver. *American Journal of Physiology-Heart and Circulatory*
969 *Physiology* **281,** H2661–H2679.
970 Mukai CN, Lathers CM, Charles JB, Bennett BS, Igarashi M & Patel S (1991).
971 Acute Hemodynamic Responses to Weightlessness During Parabolic
972 Flight. *The Journal of Clinical Pharmacology* **31,** 993–1000.

973 Neter J, Kutner MH, Nachtsheim CJ, Wasserman W & others (1996). *Applied*
974 *linear statistical models*. Irwin Chicago.
975 Newman DG & Callister R (2008). Cardiovascular Training Effects in Fighter
976 Pilots Induced by Occupational High G Exposure. *Aviat Space Environ*
977 *Med* **79,** 774–778.
978 Newman DG, White SW & Callister R (1998). Evidence of baroreflex
979 adaptation to repetitive+ Gz in fighter pilots. *Aviat Space Environ Med*
980 **69,** 446–451.
981 Norsk P (2020). Adaptation of the cardiovascular system to weightlessness:
982 Surprises, paradoxes and implications for deep space missions. *Acta*
983 *Physiologica*; DOI: 10.1111/apha.13434.
984 Norsk P, Damgaard M, Petersen L, Gybel M, Pump B, Gabrielsen A &
985 Christensen NJ (2006). Vasorelaxation in Space. *Hypertension* **47,** 69–
986 73.
987 Norsk P, Foldager N, Bonde-Petersen F, Elmann-Larsen B & Johansen TS
988 (1987). Central venous pressure in humans during short periods of
989 weightlessness. *J Appl Physiol* **63,** 2433–2437.
990 Ogawa Y, Yanagida R, Ueda K, Aoki K & Iwasaki K (2016). The relationship
991 between widespread changes in gravity and cerebral blood flow. *Environ*
992 *Health Prev Med* **21,** 186–192.
993 Ogoh S, Hirasawa A, Raven PB, Rebuffat T, Denise P, Lericollais R,
994 Sugawara J & Normand H (2015). Effect of an acute increase in central
995 blood volume on cerebral hemodynamics. *American Journal of*
996 *Physiology-Regulatory, Integrative and Comparative Physiology* **309,**
997 R902–R911.

998 Petersen LG, Damgaard M, Petersen JCG & Norsk P (2011). Mechanisms of
999 increase in cardiac output during acute weightlessness in humans. *J Appl*
1000 *Physiol* **111,** 407–411.
1001 Peterson K, Ozawa ET, Pantalos GM & Sharp MK (2002). Numerical
1002 Simulation of the Influence of Gravity and Posture on Cardiac
1003 Performance. *Ann Biomed Eng* **30,** 247–259.
1004 Pump B, Videbæk R, Gabrielsen A & Norsk P (1999). Arterial pressure in
1005 humans during weightlessness induced by parabolic flights. *J Appl*
1006 *Physiol* **87,** 928–932.
1007 Saglietto A, Tripoli F, Zwanenburg J, Biessels GJ, De Ferrari GM, Anselmino
1008 M, Ridolfi L & Scarsoglio S (2024). Role of the vessel morphology on
1009 the lenticulostriate arteries hemodynamics during atrial fibrillation: A
1010 CFD-based multivariate regression analysis. *Comput Methods Programs*
1011 *Biomed* **254,** 108303.
1012 Savarese G, Stolfo D, Sinagra G & Lund LH (2022). Heart failure with mid-
1013 range or mildly reduced ejection fraction. *Nat Rev Cardiol* **19,** 100–116.
1014 Saveko A, Bekreneva M, Ponomarev I, Zelenskaya I, Riabova A, Shigueva T,
1015 Kitov V, Abu Sheli N, Nosikova I, Rukavishnikov I, Sayenko D &
1016 Tomilovskaya E (2023). Impact of different ground-based microgravity
1017 models on human sensorimotor system. *Front Physiol* **14,** 1085545.
1018 Scarsoglio S, Fois M & Ridolfi L (2023). Increased hemodynamic pulsatility
1019 in the cerebral microcirculation during parabolic flight-induced
1020 microgravity: A computational investigation. *Acta Astronaut* **211,** 344–
1021 352.

1022 Scarsoglio S, Gallo C, Saglietto A, Ridolfi L & Anselmino M (2019).
1023 Impaired coronary blood flow at higher heart rates during atrial
1024 fibrillation: Investigation via multiscale modelling. *Comput Methods*
1025 *Programs Biomed* **175,** 95–102.
1026 Scott JM, Esch BTA, Goodman LS, Bredin SSD, Haykowsky MJ &
1027 Warburton DER (2007). Cardiovascular consequences of high-
1028 performance aircraft maneuvers: implications for effective
1029 countermeasures and laboratory-based simulations. *Applied Physiology,*
1030 *Nutrition, and Metabolism* **32,** 332–339.
1031 Shelhamer M (2016). Parabolic flight as a spaceflight analog. *J Appl Physiol*
1032 **120,** 1442–1448.
1033 Shen M & Frishman WH (2019). Effects of Spaceflight on Cardiovascular
1034 Physiology and Health. *Cardiol Rev* **27,** 122–126.
1035 Shender BS, Forster EM, Hrebien L, Ryoo HC & Cammarota JP (2003).
1036 Acceleration-induced near-loss of consciousness: The "A-LOC"
1037 syndrome. *Aviat Space Environ Med* **74,** 1021–1028.
1038 Taibbi G, Cromwell RL, Kapoor KG, Godley BF & Vizzeri G (2013). The
1039 Effect of Microgravity on Ocular Structures and Visual Function: A
1040 Review. *Surv Ophthalmol* **58,** 155–163.
1041 Tanaka K, Nishimura N & Kawai Y (2017). Adaptation to microgravity,
1042 deconditioning, and countermeasures. *The Journal of Physiological*
1043 *Sciences* **67,** 271–281.
1044 Traon AP-L, Heer M, Narici M V, Rittweger J & Vernikos J (2007). From
1045 space to Earth: advances in human physiology from 20 years of bed rest
1046 studies (1986–2006). *Eur J Appl Physiol* **101,** 143–194.

1047 Ueda K, Ogawa Y, Yanagida R, Aoki K & Iwasaki K (2015). Dose-Effect
1048 Relationship Between Mild Levels of Hypergravity and Autonomic
1049 Circulatory Regulation. *Aerosp Med Hum Perform* **86,** 535–540.
1050 Videbaek R & Norsk P (1997). Atrial distension in humans during
1051 microgravity induced by parabolic flights. *J Appl Physiol* **83,** 1862–1866.
1052 Westerhof N, Stergiopulos N, Noble MIM & Westerhof BE (2019). *Snapshots*
1053 *of Hemodynamics*. Springer International Publishing, Cham. Available
1054 at: http://link.springer.com/10.1007/978-3-319-91932-4.
1055 Whittle RS & Diaz-Artiles A (2021). Modeling individual differences in
1056 cardiovascular response to gravitational stress using a sensitivity
1057 analysis. *J Appl Physiol* **130,** 1983–2001.
1058 Widjaja D, Vandeput S, Huffel S Van & Aubert AE (2015). Cardiovascular
1059 autonomic adaptation in lunar and martian gravity during parabolic
1060 flight. *Eur J Appl Physiol* **115,** 1205–1218.
1061 Young LR & Sutton JP eds. (2021). *Handbook of Bioastronautics*. Springer
1062 International Publishing, Cham. Available at:
1063 https://link.springer.com/10.1007/978-3-319-12191-8.
1064 Zhang L-F & Hargens AR (2018). Spaceflight-Induced Intracranial
1065 Hypertension and Visual Impairment: Pathophysiology and
1066 Countermeasures. *Physiol Rev* **98,** 59–87.
1067 Zhu H, Wang H & Liu Z (2015). Effects of real and simulated weightlessness
1068 on the cardiac and peripheral vascular functions of humans: A review.
1069 *Int J Occup Med Environ Health* **28,** 793–802.
1070